The Astrophysical Journal, 668:781–795, 2007 October 20

THE MERGER IN ABELL 576: A LINE-OF-SIGHT BULLET CLUSTER?

Renato A. Dupke, Nestor Mirabal, Joel N. Bregman, and August E. Evrard
University of Michigan, Ann Arbor, MI 48109-1090
Received 2006 June 29; accepted 2007 May 22

ABSTRACT

Using a combination of *Chandra* and *XMM-Newton* observations, we confirmed the presence of a significant velocity gradient along the northeast-southwest direction in the intracluster gas of the cluster Abell 576. The results are consistent with a previous *ASCA* SIS analysis of this cluster. The error-weighted average over the ACIS-S3 and EPIC MOS1 and MOS2 spectrometers for the maximum velocity difference is $>3.3 \times 10^3$ km s^{-1} at the 90% confidence level, similar to the velocity limits estimated indirectly for the Bullet Cluster (1E 0657−56). The probability that the velocity gradient is generated by standard random gain fluctuations with *Chandra* and *XMM-Newton* is $<0.1\%$. The regions of maximum velocity gradient are in CCD zones that have the lowest temporal gain variations. It is unlikely that the velocity gradient is due to Hubble distance differences between projected clusters (probability $\lesssim 0.01\%$). We mapped the distribution of elemental abundance ratios across the cluster and detected a strong chemical discontinuity using the abundance ratio of silicon to iron, equivalent to a variation from 100% SN Ia iron mass fraction in the west-northwest regions to 32% in the eastern region. The "center" of the cluster is located at the chemical discontinuity boundary, which is inconsistent with the radially symmetric chemical gradient found in some regular clusters, but consistent with a cluster merging scenario. We predict that the velocity gradient as measured will produce a variation of the cosmic microwave background (CMB) temperature toward the east of the core of the cluster that will be detectable by current and near-future bolometers. The measured velocity gradient opens up the possibility that this cluster is passing through a near line-of-sight merger stage where the cores have recently crossed.

Subject headings: cooling flows — galaxies: clusters: individual (Abell 576, 1ES 0657−56) — intergalactic medium — X-rays: galaxies

Online material: color figures

1. INTRODUCTION

The characterization of the internal dynamics of the intracluster medium (ICM) is very important for determining the evolutionary stage of galaxy clusters (Beers et al. 1982), to study cluster formation and to assess the systematics of using clusters of galaxies as cosmological tools. The presence of surface brightness features detected by the *Chandra* satellite such as cold fronts, shock fronts, and X-ray cavities shows that the intracluster gas is often dynamically active. Furthermore, departure from assumptions such as hydrostatic equilibrium has been justified theoretically (e.g., Kay et al. 2004; Rasia et al. 2004, 2006; Pawl et al. 2005), but detection of bulk gas velocities became possible only with the launch of the *ASCA* satellite and more recently with the spectrometers on board *Chandra* and *XMM-Newton*.

The key ingredient to quantify the level of activity is the determination of gas bulk (or turbulent) velocities. In order to assess the gas dynamics we would ideally like to have a "direct" measurement of intracluster gas velocities. Since the intracluster medium is enriched with heavy elements, this can be done, for example, by measuring the Doppler shift of the spectral lines in X-ray frequencies (Dupke & Bregman 2001a, 2001b) or by measuring changes in line broadening due to turbulence (Inogamov & Sunyaev 2003; Sunyaev et al. 2003; Pawl et al. 2005). The former can currently be done only if there are enough photon counts within the spectral lines, if the instrumental gain is stable and well known, and if the instrument has good spectral resolution. Doppler shift analysis of clusters started with the *ASCA* satellite, which set constraints on bulk velocity gradients in 14 nearby clusters (Dupke & Bregman 2001a, 2001b, 2005). However, *ASCA*'s relatively high gain temporal variation limited velocity constraints to $\geq$2000 km s^{-1}, so that it is crucial to corroborate and improve previous measurements of velocity gradients found in the *ASCA* sample with those from other instruments if we wish to investigate intracluster gas dynamics.

The higher stability and better spectral resolution of the ACIS-S3 and MOS1 and MOS2 on board the *Chandra* and *XMM-Newton* satellites currently provide a unique opportunity to improve the constraints on ICM velocity gradients, allowing a factor of $\gtrsim$2 improvement in the uncertainties of velocity measurements. The two clusters found to have the most significant velocity gradients with *ASCA* were the Centaurus Cluster (Abell 3526) and Abell 576. Velocity gradients have been confirmed in the Centaurus Cluster in two off-center *Chandra* pointings (Dupke & Bregman 2006, hereafter DB06), although not confirmed with *Suzaku* (Ota et al. 2007), and here we show a combined velocity analysis of *Chandra* and *XMM-Newton* pointings of Abell 576.

Abell 576 is a richness class 1 cluster with relatively low ($T \sim$ 4 keV) central gas temperatures and average metal abundances (e.g., Rothenflug et al. 1984; David et al. 1993; Mohr et al. 1996). It has an optical redshift of 0.0389. *ASCA* velocity analysis of this cluster found a significant velocity gradient (>4000 km s^{-1}; Dupke & Bregman 2005, hereafter DB05). Evidence for dynamic activity in this cluster has been put forward in previous analyses. Rines et al. (2000, hereafter R00) determined the mass profile of Abell 576 using the infall pattern in velocity space for more than 1000 galaxies in a radius of 4 h^{-1} Mpc from the cluster's center. They found that the mass of the central megaparsec was more than twice that found from X-ray measurements, suggesting that nonthermal pressure support may be biasing the X-ray derived mass. Additional evidence for strong departures from hydrostatic equilibrium comes from energy excess of the X-ray emitting gas with respect to the galaxies (Benatov et al. 2006). These characteristics can be partially explained by nonthermal pressure support

and significant departures from spherical symmetry due to a line-of-sight merger. Mohr et al. (1996), using galaxy photometric data, found a high-velocity tail separated by $\sim$3000 km s^{-1} from the cluster's mean.

Kempner & David (2004, hereafter KD04) analyzed a *Chandra* observation of the core of this cluster and found brightness edges corresponding to mild jumps in gas density and pressure roughly in the north-south direction. The X-ray image of the cluster also shows an "arm" extending to the southwest and mild evidence of wakes ("fingers") in the north-northwest direction (Fig. 1*a*). The authors suggested that the core substructures are caused by a current merger with core velocities of $\sim$750 km s^{-1}, to maintain the gas confined across the surface brightness edge toward the north. In their scenario, the merging cluster came in from the direction of the fingers (north-northwest), has passed the core of the main cluster, created the southwest and west edges, and is now near the second core passage. In this paper, we perform a velocity analysis of Abell 576 using the full field of view covered by *Chandra*'s ACIS-S3 and combine it with two off-center observations with the *XMM-Newton* satellite using EPIC MOS1 and MOS2, specifically tailored to minimize random gain variations across the CCDs. We also present an analysis of the distributions of intracluster gas temperature, velocity, and individual elemental abundances and use them to determine the evolutionary stage of this cluster. All distances shown in this work are calculated assuming a flat universe with $H_0 = 70$ km s^{-1} Mpc^{-1} and $\Omega_0 = 1$ unless stated otherwise.

2. DATA REDUCTION AND ANALYSIS

2.1. *Chandra*

Abell 576 was observed for 39 ks on 2002 October 27 centered on ACIS-S3. Nearly a fourth of the observation was affected by flares, and we show here the analysis of the unaffected initial 29 ks of observation. We used CIAO, version 3.2.1, with CALDB, version 3.1.0, to screen the data. The data were cleaned using standard procedure.[1] Grades 0, 2, 3, 4, and 6 were used. ACIS particle background was cleaned as prescribed for VFAINT mode. A gain map correction was applied together with pulse-height analyzer (PHA) and pixel randomization. Point sources were extracted, and the background used in spectral fits was generated from blank-sky observations using the `acis_bkgrnd_lookup` script.

In order to obtain an overall distribution of the spectral parameters we developed an "adaptive smoothing" code that selects regions for spectral extraction based on a predetermined minimum number of counts, which for the cases shown here was 5000 counts cell^{-1}. The overlap of extraction regions is therefore stronger in the low surface brightness regions, away from the cluster's core. We also excluded the CCD borders by $\sim 1'$ to avoid "border effects," characteristic of these types of codes. The responses were created for each individual region with the CIAO tools `makeacisrmf` and `mkwarf`. Spectra and background spectra were generated and fitted with XSPEC, version 11.3.1 (Arnaud 1996) with an absorbed VAPEC thermal emission model. Metal abundances were measured relative to the solar photospheric values of Anders & Grevesse (1989). Galactic photoelectric absorption was incorporated using the WABS model (Morrison & McCammon 1983). Redshifts were determined through spectral fittings using a broad energy range. In the spectral fits we fixed the hydrogen column density $N_{\rm H}$ at its corresponding Galactic value of 5.7×10^{20} cm^{-2}. Spectral channels were grouped to

[1] See http://cxc.harvard.edu/ciao/guides/acis_data.html.

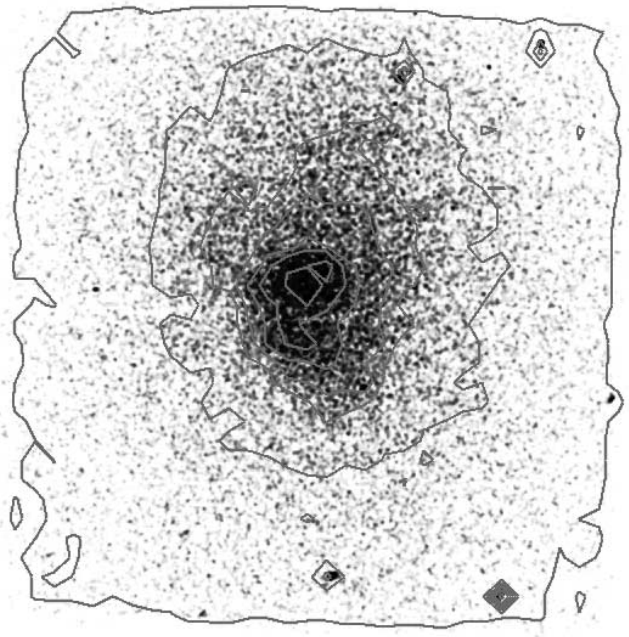

FIG. 1*a*

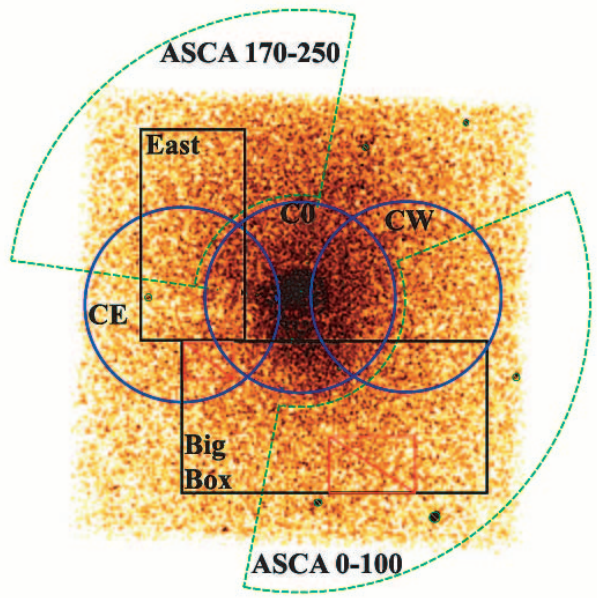

FIG. 1*b*

FIG. 1.—(*a*) Raw *Chandra* X-ray image of Abell 576. The X-ray contours shown here are used throughout the work. North is up. The lowest contour is centered at R.A. = 110.3762°, decl. = +55.7653°. The most external contour show the CCD borders and is limited by 110.5° < R.A. < 110.25° from left to right and 55.828° < decl. < 55.686° from top to bottom. The same contours are applied in Figs. 2, 5*b*, and 6*a* but with the scale slightly smaller. (*b*) Extraction regions used for spectral fittings for detailed analysis of radial velocities (South and East) and Si/Fe ratio (CW, C0, and CE) analyzed in this work. We also indicate the regions found to have high radial velocities (0°–100°) and low radial velocities (170°–250°) in a previous *ASCA* analysis (DB05). [*See the electronic edition of the Journal for a color version of this figure.*]

have at least 20 counts channel^{-1}. Energy ranges were restricted to 0.5–9.0 keV. The spectral fitting parameter errors listed here are 1 σ unless stated otherwise. For all spectral fittings used here we applied the recursive process to find the best-fit redshift with "true" χ^2 minimum, described in DB05.

2.2. *XMM-Newton*

Abell 576 was observed with *XMM-Newton* on 2004 March 23 for ~22 ks. A second observation was obtained a few days later on 2004 March 27 for a total of ~20 ks. The observations were planned in such a way as to overlap the cluster's core, while providing sufficient coverage on the northeast and southwest of the cluster, which were the regions expected to have the strongest velocity gradient from a previous *ASCA* observation (DB05; see Figs. 1*a* and 1*b*). This observational strategy was designed to minimize the impact that spatial variations of the gain (conversion between pulse height and energy of an incoming photon) has on redshift measurements.

Initial inspection of the EPIC MOS and PN data revealed a number of strong background flares. In order to exclude these periods of high background, good time intervals were produced from events where the threshold did not deviate more than 3 σ from the extrapolated mean count rate in the 10–15 keV band. In addition, only events satisfying grade patterns $\leq$12 have been used. The effective exposure times after removal of background flares correspond to ~12 ks (55% of the total) for the first pointing and ~16 ks (80% of the total) for the second. Using these cleaned event lists, background spectra were produced from several source-free regions on the detector away from the source. Blank-sky backgrounds were also used for comparison with no significant changes in the resulting best-fit parameters. The data presented here were processed with *XMM-Newton* Science Analysis System (SAS), version 6.0.0. Response files for each region have been generated using the SAS tasks `rmfgen` and `arfgen`. Bright point sources were extracted, and the spectral fitting routine was identical to that used with the *Chandra* data described in § 2.1. Only MOS1 and MOS2 were used because of the high number of interchip boundaries within our regions of interest in the PNs, which would significantly affect the estimation of gain fluctuations. Furthermore, the loss of data due to flares was especially strong for the PNs. Despite the relatively small number of counts the *XMM-Newton* observation helped to constrain the spectral parameters derived from *Chandra*.

3. PROJECTED TEMPERATURE AND VELOCITY CONTOUR MAPS

The resulting temperature and velocity distributions from the adaptive smoothing routine applied to the *Chandra* data are shown in Figures 2*a* and 2*b*. The gray scale is chosen in a way as to show the average 1 σ variation per color step.

The temperature map shows that the cluster's core regions are relatively cold (~3.5 keV) and have an overall asymmetric distribution. The coldest region (~3.0 keV) is not found in the core but in the northeast region. Interestingly, it can also be seen that the highest gas temperature is found 2′–3′ toward the northwest direction and reaches ≈5 keV. This was not noted in KD04, due to their choice of orientation for selection of the extraction regions. Overall, the temperature distribution roughly follows a configuration in which a cold core is surrounded by a hotter elliptical ring elongated along the northwest-southeast direction (Fig. 2*a*, *dashed ellipses*). There are also marginal indications that the temperature decreases again at regions >3′ to the east and south directions.

The velocity map (Fig. 2*b*) is not smooth and shows higher velocities in the southern regions, and a clear zone of lower redshifts to the northeast that extends to the central region. Even though the highest redshift zone is apparently in the southeast corner, analysis of the error map in Figure 2*c* shows that region has very high uncertainties. To find the regions of maximum significance of velocity measurements, in each cell we divided the difference of the best-fit redshift from the average over the CCD (denoted by angle brackets) by the error of the measured redshift δz, i.e., $(z - \langle z \rangle)/\delta z$ (see DB05, DB06 for details). We denote this error-weighted deviation simply as the deviation significance and plot its gray-scale contours in Figure 2*d*, where the black and white represent negative and positive velocities, respectively, with respect to the CCD average velocity. The magnitude of the deviation significance shows how significant the velocity structure is. We can see that the region of maximum negative significance is located slightly to the east of the cluster center. There is also a region of marginally higher positive significance (~3 σ) to the southwest, in good agreement with previous observations with *ASCA*. Based on these two deviation significance peaks we selected two regions for a more detailed study, shown in Figure 1*b* as black rectangles; high (redshifted) and low (blueshifted) redshift regions, hereafter called "South" and "East," respectively. Although the cluster core seems to be included in the blueshifted zone in both *Chandra* and *XMM-Newton* (and was also in the *ASCA* SISs), we conservatively avoid including it in our velocity analysis due to modeling uncertainties (see DB05 for a more extended discussion on the impact of multiple spectral models in the best-fit redshift with the technique used here). Below we explore in more detail the spectral analysis of these regions.

4. *CHANDRA* AND *XMM-NEWTON* VELOCITY ANALYSIS OF SELECTED REGIONS

The best-fit gas temperatures, iron abundances, and velocities for the two regions with the highest deviations from the average redshift are plotted in Figure 3*a* and listed in Table 1. The spectra corresponding two these two regions are shown in Figures 3*b*, 3*c*, and 3*d*, for different spectrometers. Individual spectral fits of these regions show very similar gas temperatures, with an error-weighted average of 3.87 ± 0.11 keV for South and 4.00 ± 0.11 keV for East, and similar iron abundances, with an error-weighted average of 0.54 ± 0.06 solar for South and 0.52 ± 0.05 solar for East.

However, they show very discrepant radial velocities. With *Chandra*, South shows a best-fit redshift of $(3.71^{+0.24}_{-0.60}) \times 10^{-2}$, consistent with the overall redshift determined optically (0.039 ± 0.0003; Mohr et al. 1996[2]). The East region shows a much lower best-fit redshift of $\lesssim$0.016 (the lower limits are not well constrained and are consistent with 0), implying a velocity difference of >3900 km s^{-1} at the 90% confidence level. The velocity difference is consistent and better constrained than those obtained for similar regions with the *ASCA* spectrometers.

XMM-Newton MOS1 and MOS2 analysis of the same regions shows a similar velocity gradient. With MOS2 the upper limit of the redshift values of the East region is not well constrained (there is a secondary χ^2 minimum for the best-fit redshift at ~0.035). Since the overall results are very consistent between the two MOS detectors, we fitted MOS1 and MOS2 spectra simultaneously to improve statistics. The results of the simultaneous fittings are also displayed in Table 1. The best-fit redshift difference between these two regions is found to be >4000 km s^{-1} at the 90% confidence level.

[2] Including all galaxy subpopulations discussed in Mohr et al. (1996).

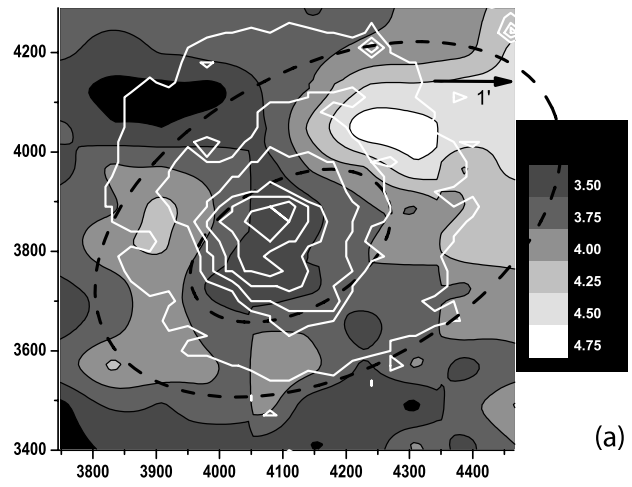

FIG. 2*a*

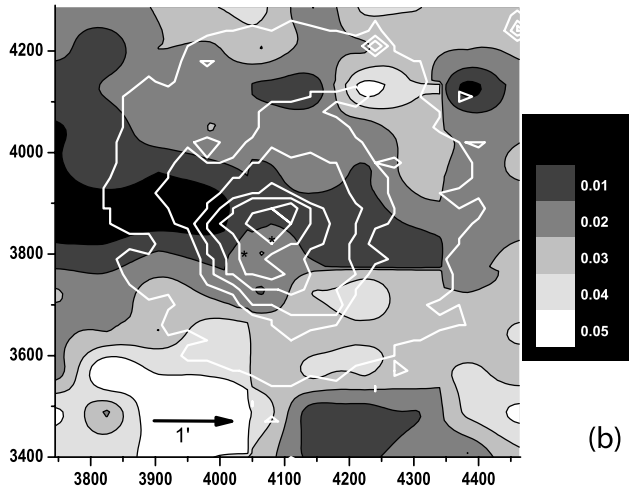

FIG. 2*b*

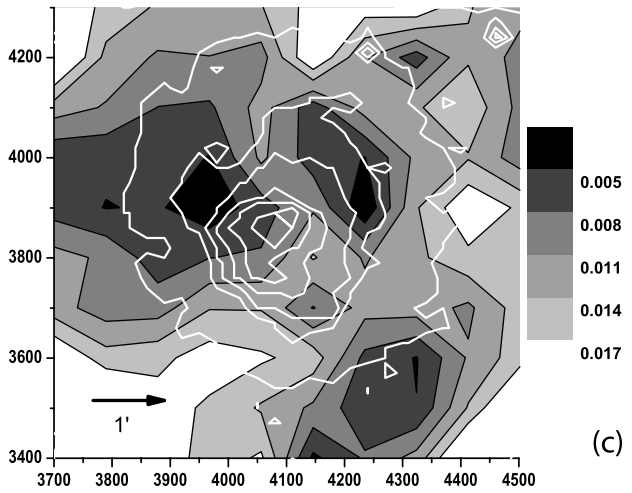

FIG. 2*c*

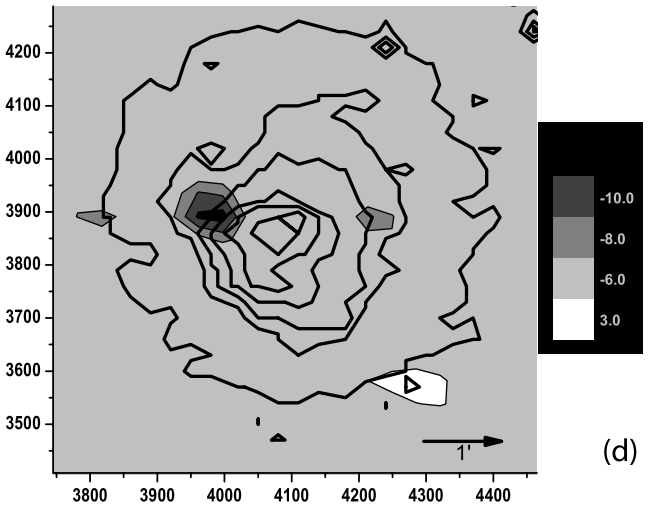

FIG. 2*d*

FIG. 2.—Results from an adaptive smoothing algorithm with a minimum of 5000 counts per extraction circular region and fitted with an absorbed VAPEC spectral model. The gridding method used is a correlation method that calculates a new value for each cell in the regular matrix from the values of the points in the adjoining cells that are included within the search radius. With the minimum count constraints the matrix size was 50×50 cells. We also overlay the X-ray contours shown in Fig. 1*a* on top of the gray-scale contour plot. North is up. The lowest contour is centered at R.A. $= 110.3762^{\circ}$, decl. $= +55.7653^{\circ}$. The units are pixels and 1 pixel $= 0.5''$. The arrow indicates $1'$. The parameters mapped are (*a*) temperature, (*b*) redshift, (*c*) smoothed redshift error of each cell used in the adaptive binning, and (*d*) deviation significance $(z - \langle z \rangle)/\delta z$, i.e., redshift value found in (*b*) minus the average for the whole CCD divided by the error of each measurement. The dashed ellipses shown in the temperature plot in (*a*) indicate approximately the direction of the Mach cone in the scenario of a near line-of-sight merger. The two asterisks near the center of the redshift map in (*b*) indicate the position of two bright E galaxies near the cluster's X-ray center, with relative line-of-sight velocity difference of 900 km s^{-1} (Smith et al. 2000). The average redshift error for each cell used in the adaptive binning code is 0.01. The errors for the cells near the bottom left (southeast) regions reach 0.02.

We can assess the statistical uncertainties of the velocity differences between these two region using the *F*-test, i.e., fitting the spectra of the two regions simultaneously with the redshifts locked together and comparing the resulting χ^2 to that of simultaneous fittings where the redshifts are allowed to vary independently. The *F*-test indicates that the velocity differences in these two regions are significant at the 99.8% and 97.6% confidence level for *Chandra* ACIS-S3 and MOS1 + MOS2, respectively. The error-weighted average velocity difference from all three detectors is $(5.9 \pm 1.6) \times 10^3$ km s^{-1} (the errors are 1 σ).

4.1. *Inclusion of Gain*

The significance of the velocity gradient described above only includes statistical uncertainties. The major source of uncertainty in velocity measurements with current X-ray spectrometers is the temporal and spatial variations of the instrumental gain. As in DB06, we can estimate the effects of residual gain fluctuations through Monte Carlo simulations. Given the relatively early date of the observations, we used the study of the gain variations in the first 20 rows of *Chandra* ACIS-S3 by Grant (2001) and assume that they also represent the expected variation for MOS1 and MOS2 as well. For a discussion on the gain stability in the *XMM-Newton* detectors see Andersson & Madejski (2004).

In order to assess the impact that random gain fluctuations would have on our results we simulated 500 spectra for *Chandra*'s ACIS-S3 and *XMM-Newton*'s MOS1 and MOS2 using the XSPEC tool `fakeit`. The simulated spectra had the same input values as those obtained through spectral fittings of the real data

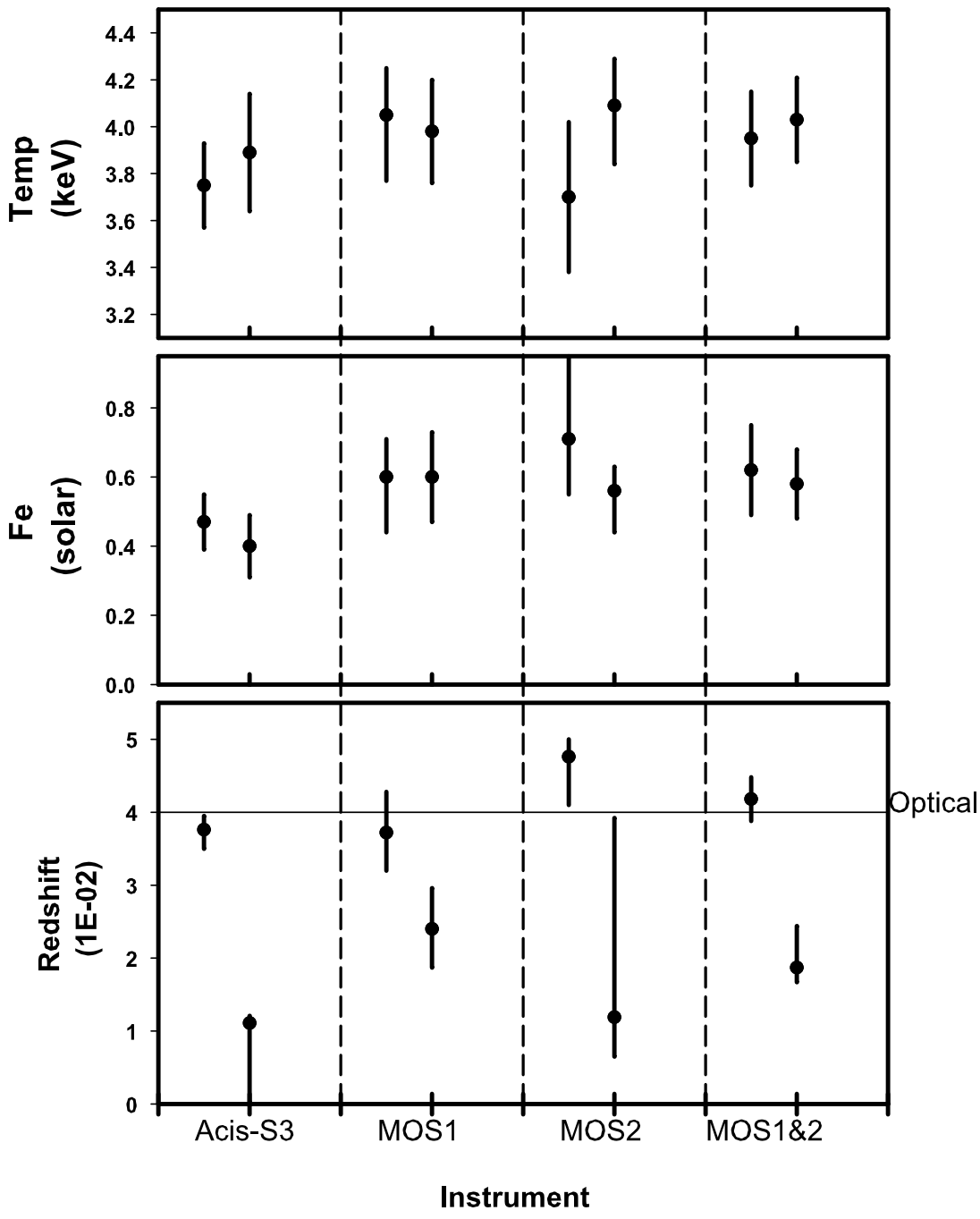

FIG. 3*a*

FIG. 3.—(*a*) Best-fit values for temperature, Fe abundance, and redshift for the South and East regions shown in Fig. 1*b* with different instruments. The left data point for each instrument shows the value for South and the right data point the value for East. "MOS1&2" represents the results from simultaneous spectral fittings of the two MOS spectrometers. We also indicate the optically determined redshift for the cluster. (*b*) *Top*: Spectral fittings for regions SOUTH (*white*) and EAST (*gray*) using *Chandra* ACIS-S3 data. *Bottom*: Blowup of the more prominent lines in the Fe L and K complexes with the continuum subtracted. (*c*) Same as (*b*) but for the MOS1 data. (*d*) Same as (*b*) but for the MOS2 data. [*See the electronic edition of the Journal for color versions of this figure*.]

in the South and East regions for $N_{\rm H}$, temperature, oxygen, neon, magnesium, silicon, sulfur, argon, calcium, iron, nickel, and normalization and were set at some intermediary redshift ($z = 0.029$). The background and responses corresponded to those of the real data. Poisson errors were included. The simulated spectra were then used to estimate the probability that a velocity difference similar to or greater than that observed in the real data in ACIS-S3, MOS1, and MOS2 could be generated by chance and how this probability depended on the magnitude of the gain fluctuations. The results are shown in Figure 4*a*, where we plot the probability that $c(z_{\rm South} - z_{\rm East}) > \Delta V$ as a function of the 1 σ variation of the gain (assumed 300 km s^{-1} for individual velocity measurements; Grant 2001).[3] We can see from Figure 4*a* that the significance of the velocity gradient is >99% assuming a 3 σ gain variation.

[3] There is evidence that both spatial and temporal variations are larger at later times (DB06).

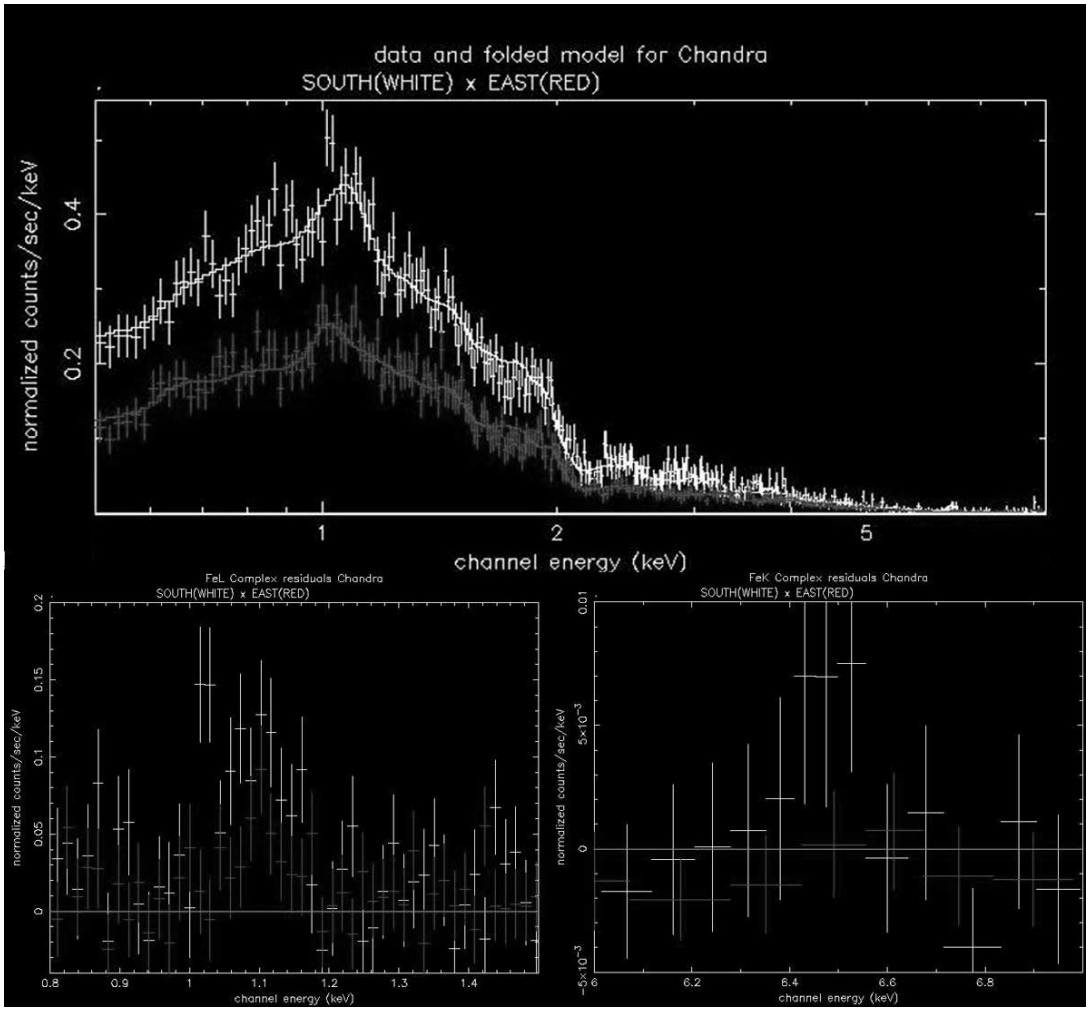

FIG. 3*b*

4.2. *Temporal and Spatial Gain Stability*

The two *XMM-Newton* pointings from which the extraction regions were analyzed were taken with a separation of four days. We checked for possible anomalous gain variations that might have occurred between the two off-center observations by using a large elliptical region surrounding the cluster's center, discussed in § 6.2 (see Fig. 2*a*, *outer dashed ellipse*). We fitted an absorbed APEC model and checked for redshift differences between different epochs in MOS1 and MOS2 data individually. The best-fit redshifts in the two epochs for MOS1 are $(3.98 \pm 0.39) \times 10^{-2}$ and $(3.61 \pm 0.26) \times 10^{-2}$. For MOS2 the corresponding values are $(3.56 \pm 0.39) \times 10^{-2}$ and $(3.66 \pm 0.13) \times 10^{-2}$. There were no significant changes in best-fit global redshift between the two observations or between different detectors.

Given the random variation of instrumental gain with position and time in the CCDs, it is useful to check whether some particular CCD region has been more affected than others. As in DB06, we split the cleaned final ACIS-S3 event file into three different epochs (with ~9.7 ks each) and performed the same velocity mapping as that described previously, i.e., through an adaptive smoothing routine that keeps a fixed minimum number of counts per region (5000 counts) maintaining the range of fitting errors more or less constant for different regions. We then determined the standard deviation of the best-fit velocities for the same region over different time periods. We plot the results in Figure 4*b*, where regions of high scatter are lighter. The gray-scale steps in Figure 4*b* represent the average 1 σ fitting errors of the individual regions used to construct the velocity map. From Figure 2*d*, we can see that the regions of significant low and high velocities are located in the zones with minimum redshift scatter ($\sigma_z \sim 0.004$). This suggests that the velocity gradient is not dominated by local temporal variations of the gain. ACIS-S3 was the only instrument with enough counts to perform this analysis, given the loss of photons to flares with the *XMM-Newton* data.

5. INDIVIDUAL LINES AND ABUNDANCE RATIOS

Elemental abundance ratios can be used to determine the enrichment history of the intracluster gas (e.g., Mushotzky et al. 1996; Loewenstein & Mushotzky 1996) and can potentially be used to characterize the ICM and to trace the origin of the undisturbed gas during merging (e.g., Dupke & White 2003). This is because the internal variation of these ratios is not random, but typically shows a central dominance of Type Ia supernova (SN Ia) ejecta (Dupke & White 2000a, 2001b; Finoguenov et al. 2000; Allen et al. 2001).[4] Dupke & White (2003) have used the "lack" of a chemical discontinuity in some cold fronts to point out that the scenario that cold fronts are caused by the unmixed remnant core of an accreted subsystem (Markevitch et al. 2002) is not the

[4] Here we use the term "SN type dominance" to denote SN type Fe mass fraction, not to be confused with the actual number of SNe.

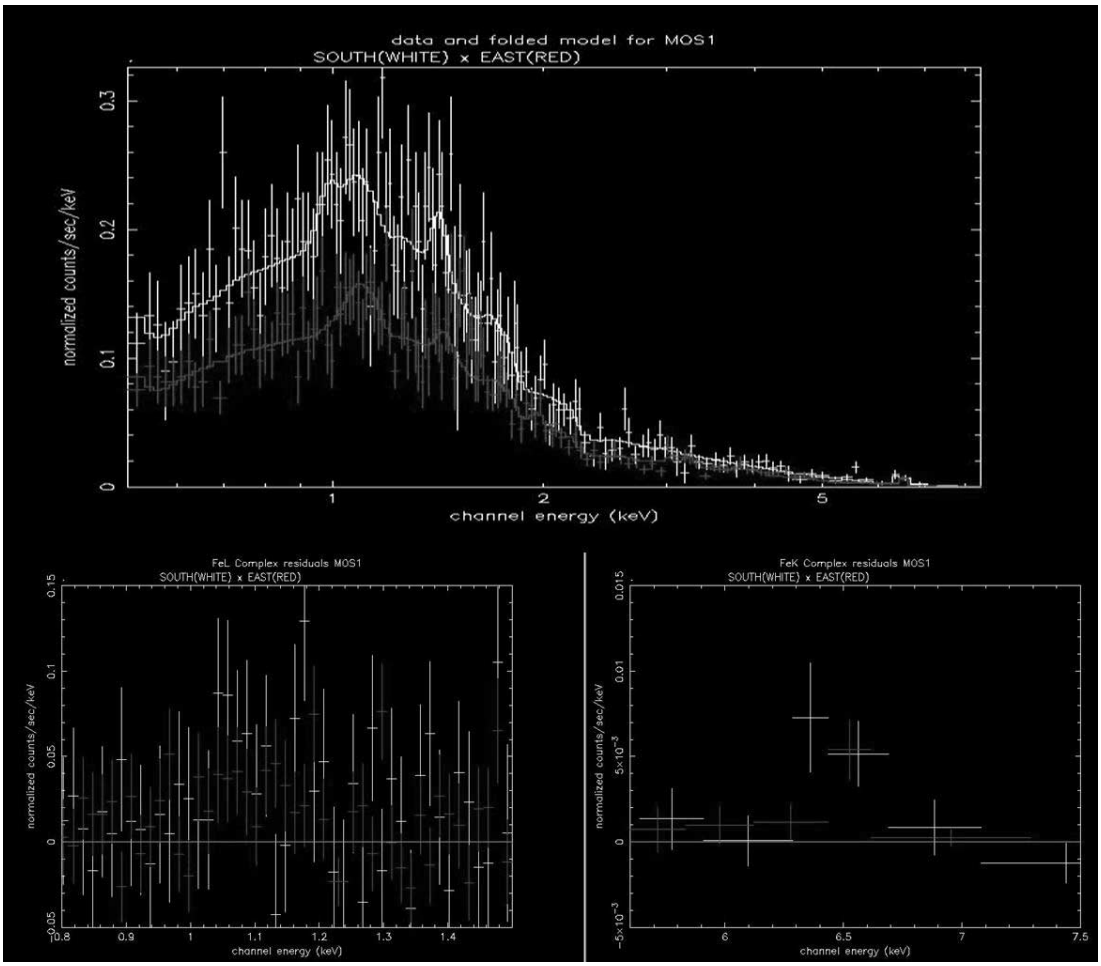

FIG. 3*c*

unique way to make cold fronts. Here we use abundance ratios to test the merging scenario, i.e., to look for a discontinuity that separates two different media with different enrichment histories.

Given the low temperatures and poor photon statistics for both *Chandra* and *XMM-Newton* observations, the abundances of silicon and iron are the best defined and isolated lines in the X-ray spectra in our usable frequency range. The Si/Fe ratio spans a relatively wide range of values between SN Ia and SN II yields, even when taking into account the theoretical yield uncertainties of different SN models (Gibson et al. 1997; Dupke & White 2000a, 2000b). Using the same adaptive smoothing routine as described above we mapped the Si/Fe ratio throughout the cluster region with ACIS-S3. The results are shown in Figure 5*a*. The cluster's core sits on a clear separation between two media, highly discrepant in SN type dominance. The Fe mass fraction toward the west and northwest is strongly dominated by SN Ia ejecta, while the east side is dominated by SN II ejecta. The transition from SN Ia to SN II dominance is nearly centered along the arrow-shaped brightness edge.

Based on the Si/Fe *Chandra* map we selected three characteristic regions for a direct comparison of the chemical enrichment gradient measured with *Chandra* and *XMM-Newton*. These regions are circular and are denoted as CW (circle west), C0 (circle center), and CE (circle east) in Figure 1*b*. Individual silicon and iron abundances are shown in Table 2, and their ratios derived from different instruments are plotted in Figure 5*b*. In Figure 5*b* we also show the theoretical limits for 100% SN II Fe mass fraction (*top horizontal line*) and 100% SN Ia Fe mass fraction for four theoretical supernova explosion models that differ in their explosion characteristics (*bottom horizontal lines*; Nomoto et al. 1997a, 1997b). The error-weighted average of the SN Ia Fe mass fraction contribution for CW is found to be $100^{+0.00}_{-0.09}$% as opposed to 33% $\pm$ 22% found for the CE region.

6. DISCUSSION

In this work we reanalyzed the *Chandra* observation of Abell 576 and determined the spatial distribution of temperatures, individual elemental abundances, and radial velocities of the ICM, using the full field of view of the ACIS-S3 and two new *XMM-Newton* observations covering similar spatial scales. This allowed us to compare the results obtained with different instruments having different systematic uncertainties. The velocity distribution near the core of the cluster shows a strong velocity gradient, in very good agreement in both magnitude and direction with the velocity gradient found with both SISs on board *ASCA*. The error-weighted average (over ACIS-S3, MOS1, and MOS2) maximum velocity difference is found to be $(5.9 \pm 1.6) \times 10^3$ km s^{-1}. The combined set of observations makes the significance of velocity detection >99.9% confidence, when standard ($1\ \sigma$) gain fluctuations are taken into account.

We also found a strong chemical gradient in the intracluster gas of this cluster. The distribution of iron and silicon abundances is asymmetric in such a way as to produce a clear separation of the Si/Fe ratio at the cluster's center. If converted to SN type

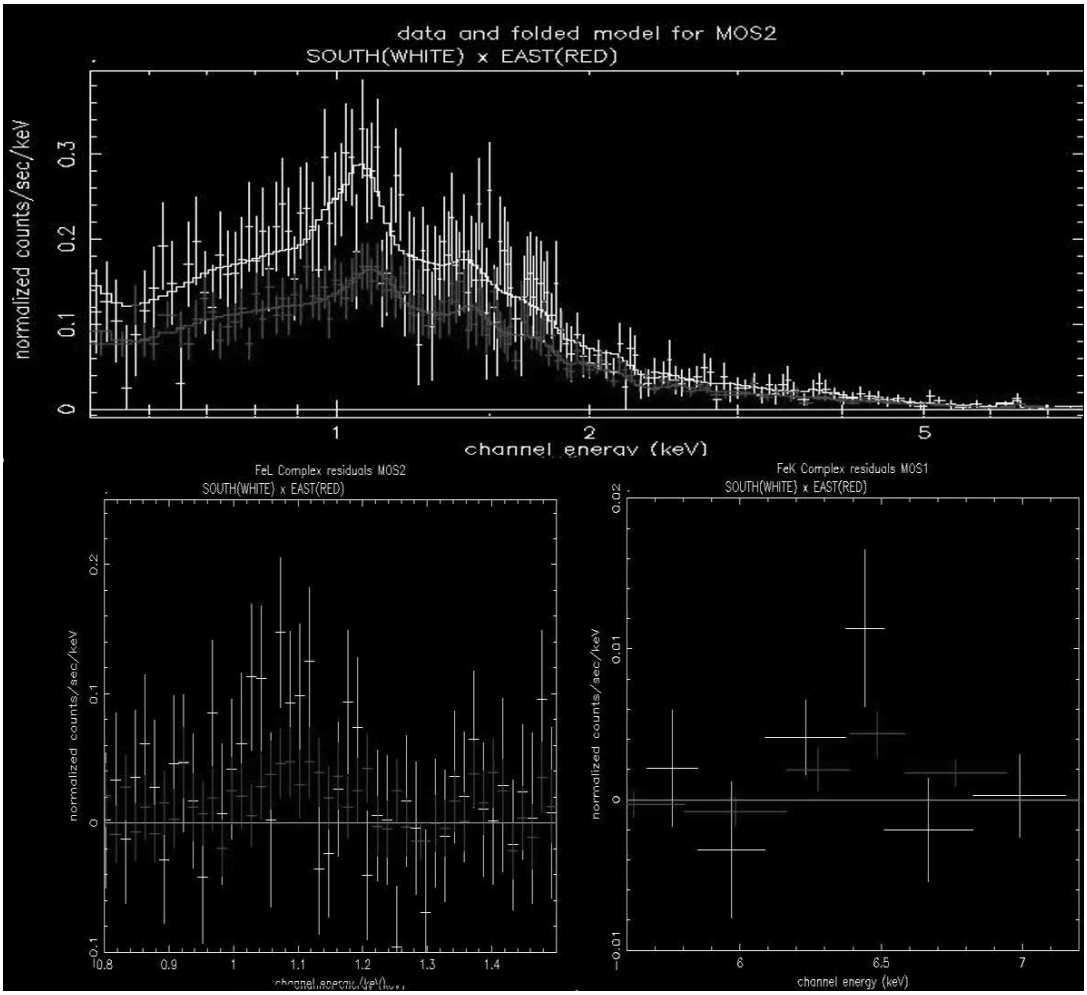

FIG. 3*d*

enrichment, the results indicate that nearly 67% of the Fe mass has been produced by SNe II toward the east and that the Fe mass content in the ICM toward the west and northwest directions has been fully produced by SNe Ia (<9% produced by SNe II). This chemical gradient is very asymmetric, not consistent with the radial chemical gradients found in some other clusters (e.g., Dupke 1998; Dupke & White 2000a, 2000b, 2003; Finoguenov et al. 2000; Allen et al. 2001; De Grandi et al. 2004; Baumgartner et al. 2005). The general characteristics of this cluster are consistent with a merging origin as proposed by KD04. However, the velocity gradient in Abell 576 suggests a larger line-of-sight component for the merger axis.

TABLE 1
SPECTRAL FITTINGS FOR SOUTH AND EAST REGIONS

Instrument	Temperature (keV)	Abundance[a] (Solar)	Redshift (10^{-2})	χ^2/dof
South Region				
Chandra	3.75 ± 0.18	0.47 ± 0.08	$3.71^{+0.24}_{-0.60}$	578/398
MOS1	$4.05^{+0.20}_{-0.28}$	$0.60^{+0.11}_{-0.16}$	$3.72^{+0.56}_{-0.52}$	728/429
MOS2	3.70 ± 0.32	$0.71^{+0.26}_{-0.16}$	$4.76^{+0.24}_{-0.66}$	728/429
MOS1 and MOS2	3.95 ± 0.20	0.62 ± 0.13	4.18 ± 0.30	728/429
East Region				
Chandra	3.89 ± 0.25	0.40 ± 0.09	$1.11^{+0.48}_{-1.08}$	341/314
MOS1	3.98 ± 0.22	0.60 ± 0.13	$2.40^{+0.56}_{-0.53}$	541/362
MOS2	$4.09^{+0.20}_{-0.25}$	$0.56^{+0.07}_{-0.12}$	$1.19^{+2.73}_{-0.54}$	541/362
MOS1 and MOS2	4.03 ± 0.18	0.58 ± 0.10	$1.87^{+0.57}_{-0.20}$	541/362

NOTES.—Errors are 1 σ confidence. Values are across the full energy range (0.5–9.5 keV).
[a] Photospheric.

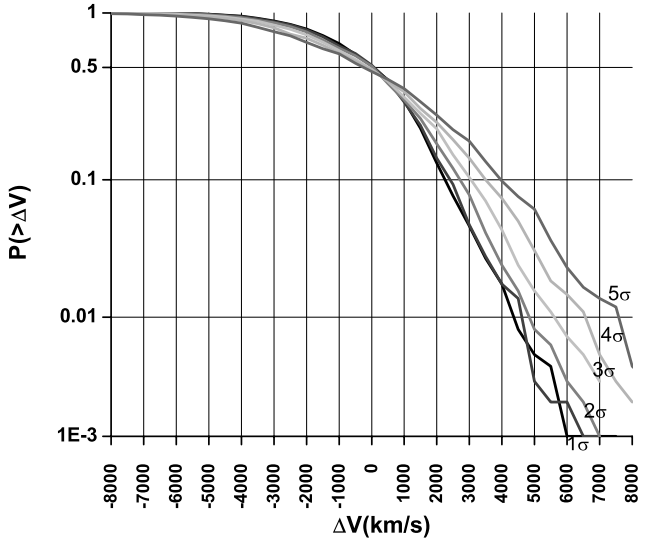

FIG. 4*a*

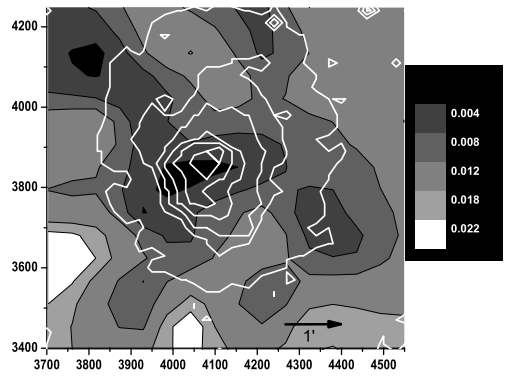

FIG. 4*b*

FIG. 4.—(*a*) Probability of detecting a velocity difference greater than ΔV for the South and East regions. The black line shows the case without gain fluctuations. The other lines assume a 1, 2, 3, 4, and 5 σ gain fluctuation (1 $\sigma \approx 500$ km s^{-1} for individual velocity differences). Results are obtained from spectral fittings of 500 simulated spectra for each region for *Chandra* and *XMM-Newton*. (*b*) Smoothed map of the scatter (standard deviation) of the best-fit redshifts over three time cuts (epochs), each having 9.7 ks duration. Darker regions indicate lower scatter and therefore higher gain stability. We also overlay the X-ray contours shown in Fig. 1*a* on top of the contour plot. North is up. The lowest contour is centered at R.A. = 110.3762°, decl. = +55.7653°. The units are pixels and 1 pixel = 0.5″. The arrow indicates 1′. [*See the electronic edition of the Journal for a color version of this figure*.]

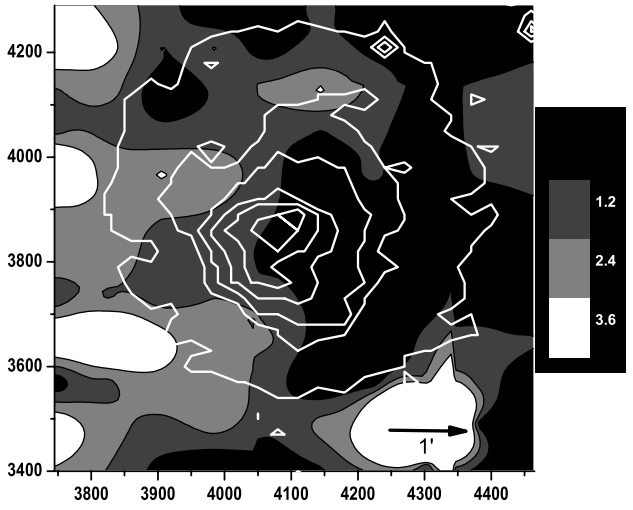

FIG. 5*a*

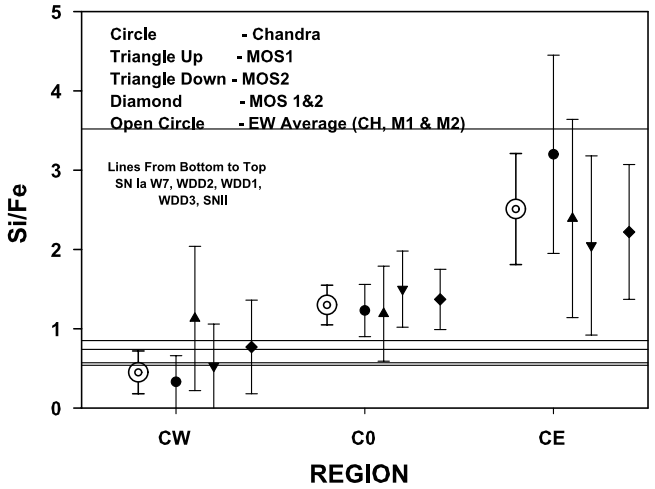

FIG. 5*b*

FIG. 5.—(*a*) Results from an adaptive smoothing algorithm described in Fig. 2 for the Si/Fe abundance ratio found with *Chandra* data. We also overlay the X-ray contours shown in Fig. 1*a* on top of the contour plot. North is up. The lowest contour is centered at R.A. = 110.3762°, decl. = +55.7653°. The units are pixels and 1 pixel = 0.5″. The arrow indicates 1′. (*b*) Si/Fe abundance ratio measurements (by number normalized to solar) of regions CW, C0, and CE using *Chandra* and *XMM-Newton* MOS1, MOS2, and MOS1 and MOS2 combined. We also shown the theoretical predictions for pure SN II enrichment (*top horizontal line*) and different models of pure SN Ia enrichment (standard W7 and delayed detonation models 1, 2, and 3 of Nomoto et al. 1997a, 1997b).

The distribution of galaxy velocities in the field of Abell 576 does not show any clear spatial segregation (R00), as typically seen in optically selected rotating cluster candidates (Hwang & Lee 2007). However, the distribution of galaxies (from the NED database[5]) with redshift within r_{200} shows at least two large concentrations between $0.03 < z < 0.07$ (Fig. 6*a*). The first one is centered at $z \sim 0.0387$, which is the characteristic cluster redshift. We separate three galaxy groups based on redshift: a low-z group ($0.03 < z < 0.0387$), a high-z group ($0.0387 < z < 0.05$), and a very high z group ($0.057 < z < 0.07$). We plot the galaxies for these three groups in Figures 6*b* and 6*c*. It can be seen from Figure 6*b* that the distribution of the 97 low-z galaxies (*blue*) seem more isotropic than that of the 76 high-z galaxies (*red*), which seems to be more concentrated toward the southwest of the cluster. The distribution of the 24 very high z galaxies (*magenta*) is displaced even more to the southwest. Figure 6*c* shows a blowup of Figure 6*b* with the velocity centroids of the three redshift groups (*crosses with the corresponding group colors*). The velocity centroids are 2.4′ (2.2′) away from the X-ray center for the low (high) z group. The X-ray center is also $\gtrsim$1.3′ from the line connecting the centroids of the two groups. This difference is significantly out of the error ellipsoid for the velocity centroid (assuming 6×10^{-5} and 2.5″ errors for redshift and position, respectively [NED]).

It is very difficult to make a direct comparison between the velocity measurements obtained from galaxy velocities and X-ray measurements given the difference of spatial scales. In general,

[5] Available at http://nedwww.ipac.caltech.edu.

TABLE 2
Individual Elemental Abundances

Instrument	Silicon (Solar)	Iron (Solar)	Si/Fe
CW Region			
Chandra	0.26 ± 0.26	0.80 ± 0.12	0.33 ± 0.33
MOS1	0.59 ± 0.46	0.52 ± 0.11	1.13 ± 0.91
MOS2	0.32 ± 0.32	0.61 ± 0.09	0.53 ± 0.53
MOS1 and MOS2	0.44 ± 0.33	0.58 ± 0.9	0.77 ± 0.59
C0 Region			
Chandra	0.89 ± 0.23	0.73 ± 0.07	1.23 ± 0.33
MOS1	0.66 ± 0.32	0.55 ± 0.08	1.19 ± 0.60
MOS2	1.07 ± 0.32	0.71 ± 0.08	1.50 ± 0.48
MOS1 and MOS2	0.85 ± 0.22	0.62 ± 0.5	1.37 ± 0.38
CE Region			
Chandra	1.38 ± 0.38	0.43 ± 0.12	3.20 ± 1.25
MOS1	1.01 ± 0.47	0.42 ± 0.11	2.39 ± 1.25
MOS2	0.90 ± 0.45	0.44 ± 0.10	2.05 ± 1.13
MOS1 and MOS2	0.95 ± 0.33	0.43 ± 0.07	2.22 ± 0.85

Note.—Errors are 1 σ confidence.

the optical results are not inconsistent with the X-ray measurements. However, the absolute values between the redshifts of the galaxy concentrations and those obtained from X-ray spectroscopy are discrepant, and the results can only be compatible if there is an overall gain correction upward. We do not have an external source to calibrate global gain corrections, but it is unlikely that the same correction would affect all three different instruments in different epochs. On the other hand, the methodology used here is sensitive to gain dependence on frequency (e.g., Dupke & Bregman 2001b), and this is likely the reason for this discrepancy given the low temperatures of the cluster (the redshift fitting process is weighted by the Fe L complex). Even though the *absolute* redshift values may be inaccurate, the redshift *differences* should not be affected, since the same methodology was applied to all regions and observations. So we will assume that a correction of $\delta z \sim 0.015$–0.02 should be applied to all measured redshifts when comparing the data in X-ray and optical frequencies.

The relative orientation of the low- and high-velocity regions is very similar to that found in X-ray velocity measurements (northeast-southwest). We also show the centroid of the joint high and very high z group as a yellow cross. The centroid of this group coincides with the most significant high-velocity region (Fig. 2*d*). The above-mentioned results using galaxy velocities can also be interpreted as due to an unusual amount of interlopers (e.g., Wojtak & Loas 2007), and in this section we discuss two scenarios that can explain the observations, i.e., projection of a background cluster and post–core crossing line-of-sight merging.

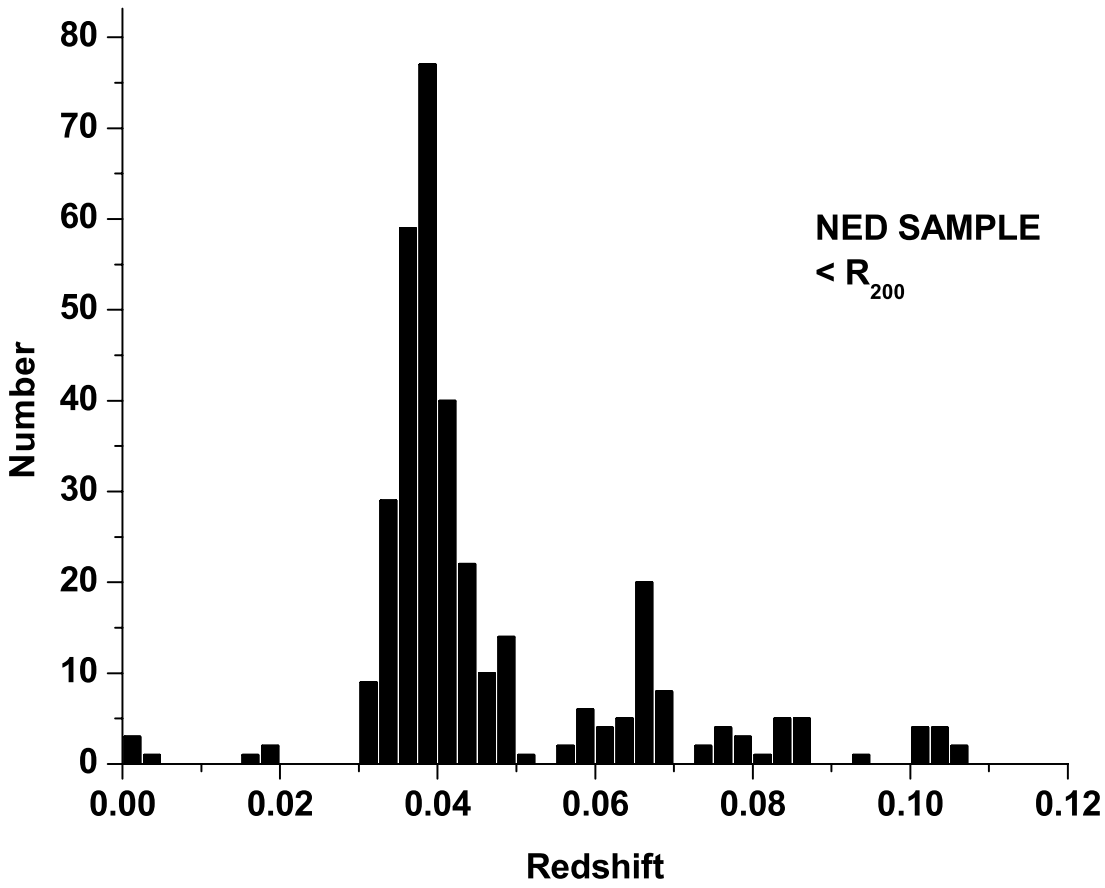

Fig. 6*a*

Fig. 6.—(*a*) Histogram of galaxy velocities within a projected distance of $1r_{200}$ from the X-ray center. Data are from NED. (*b*) Galaxy positions separated by redshift in the histogram shown in (*a*). Galaxies with redshifts $0.03 < z < 0.0387$ are denoted by blue circles. Red circles denote galaxies with redshifts $0.0387 < z < 0.05$, and magenta circles correspond to $0.057 < z < 0.07$. X-ray contours are also shown in the center of the figure in white, and the South and East rectangular regions are shown in green. The large black circle corresponds to $\sim 1r_{200}$. (*c*) Blowup of Fig. 6*b*. Notation is the same as in (*b*). Crosses show the velocity centroids for different redshift groups: Blue corresponds to $0.03 < z < 0.0387$, red to $0.0387 < z < 0.05$, magenta to $0.057 < z < 0.07$, and yellow to $0.0387 < z < 0.07$.

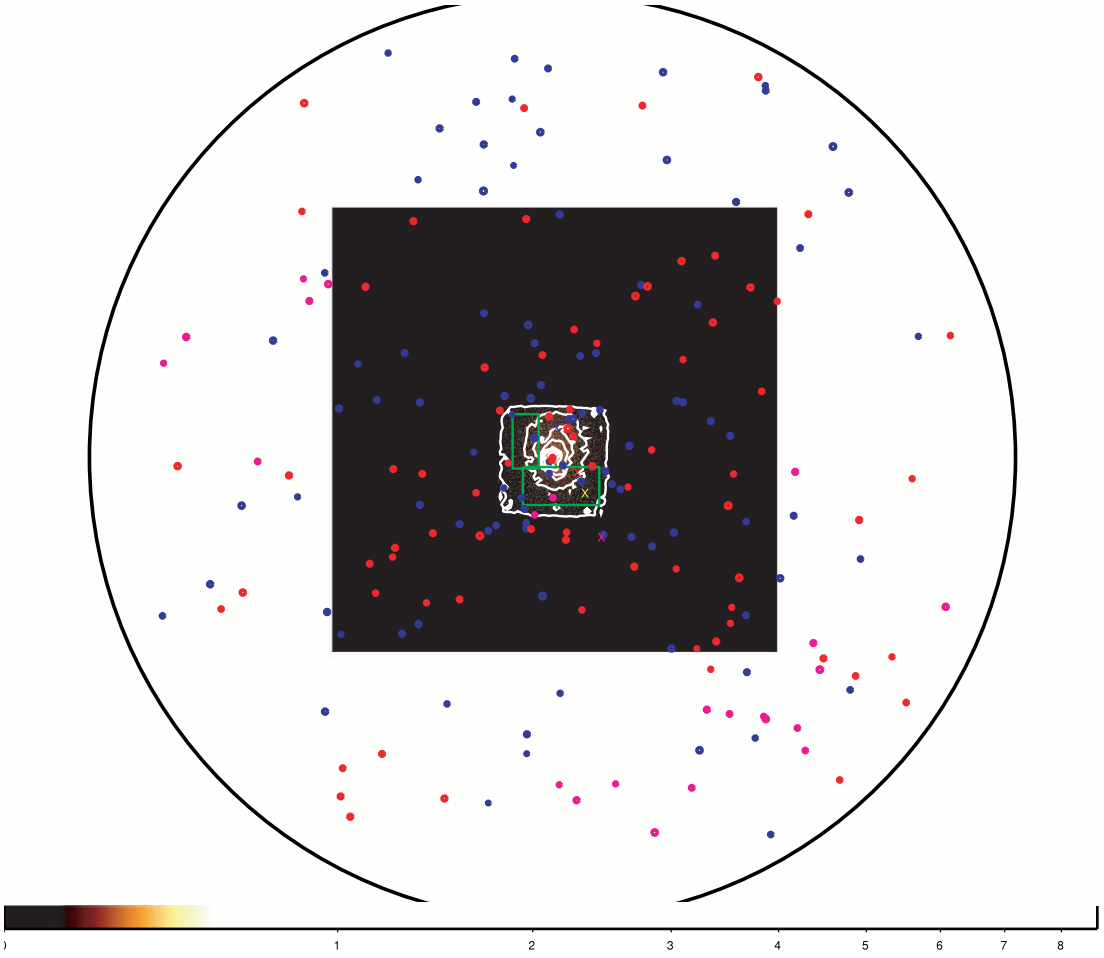

FIG. 6*b*

6.1. *Projection Scenario*

The results presented above can be at least partially interpreted as resulting from a scenario in which Abell 576 is, in reality, two clusters closely aligned in the line of sight. The two clusters could be gravitationally unbound or in a premerger stage, in which case the velocity gradient would be mostly attributed to the clusters' Hubble distances. In this scenario the cores of both clusters would have to be nearly aligned in order to escape easy identification of a secondary peak in surface brightness.

Optical studies of Abell 576 show several peculiarities that can be interpreted either as consequences of a cluster-cluster merging or as due to projection effects. R00 used the kinematics of the infall region (Diaferio & Geller 1997) of Abell 576 to calculate the mass distribution out to several megaparsecs. Their method does not need the equilibrium assumptions typically used in X-ray mass estimates and relies on the fact that the velocity field around clusters is determined by the local dynamics of the dark matter halo. The amplitude of the characteristic trumpet-shaped caustics in their velocity times radius plot is related to the escape velocity around halos. From their analysis, one can infer that this cluster is passing through a major disturbance: (1) there is a "finger" in phase space with high velocities for radii $<2.9\,h_{70}^{-1}$ Mpc (Fig. 4 of R00; see also Rines et al. 2003; Rines & Diaferio 2006); (2) there is an apparent deficit of galaxies in the northwest of the cluster (Fig. 6 of R00); (3) there is a similar geometrical configuration of a high-velocity "background" system (centered nearly 8200 km s^{-1} over the cluster's redshift) to the geometrical configuration of the cluster (Figs. 14 and 6 of R00), suggesting a physical connection between the cluster and the background system; and (4) there is an inferred total mass 2.5 times higher than that found from X-ray analysis within the same spatial scales (see also Mohr et al. 1996).

In order to estimate the likelihood that the velocity gradient is due to projection effects we looked at the distribution of galaxy clusters from cosmological *N*-body Hubble volume simulations. For that we use the positions of clusters in a 3 Gpc cube at $z \approx 0$ selected in the data generated in Evrard et al. (2002). The virtual clusters were generated in a flat ΛCDM model, with Ω_m and Ω_Λ of 0.3 and 0.7, respectively and $\sigma_8 = 0.9$. Clusters were found using an algorithm that identifies halos as spheres, centered on local density maxima, with radii defined by a mean interior isodensity condition (see Appendix A of Evrard et al. 2002 for details).

We searched within 500,000 mock clusters for those that had a projected core separation within 180 h_{70}^{-1} kpc, corresponding to 3.5′ at a redshift ∼0.04. To be conservative we searched for a radial distance separation within 2 σ above and below the average redshift difference value of $(5.9 \pm 1.6) \times 10^3$ km s^{-1}. The results showed 265 systems that satisfied this criterion indicating a probability of 5×10^{-4} of finding such systems in the nearby universe.

6.2. *Merging Scenario*

Local mergers are, however, much more frequent. The same above-mentioned Monte Carlo strategy applied to angular

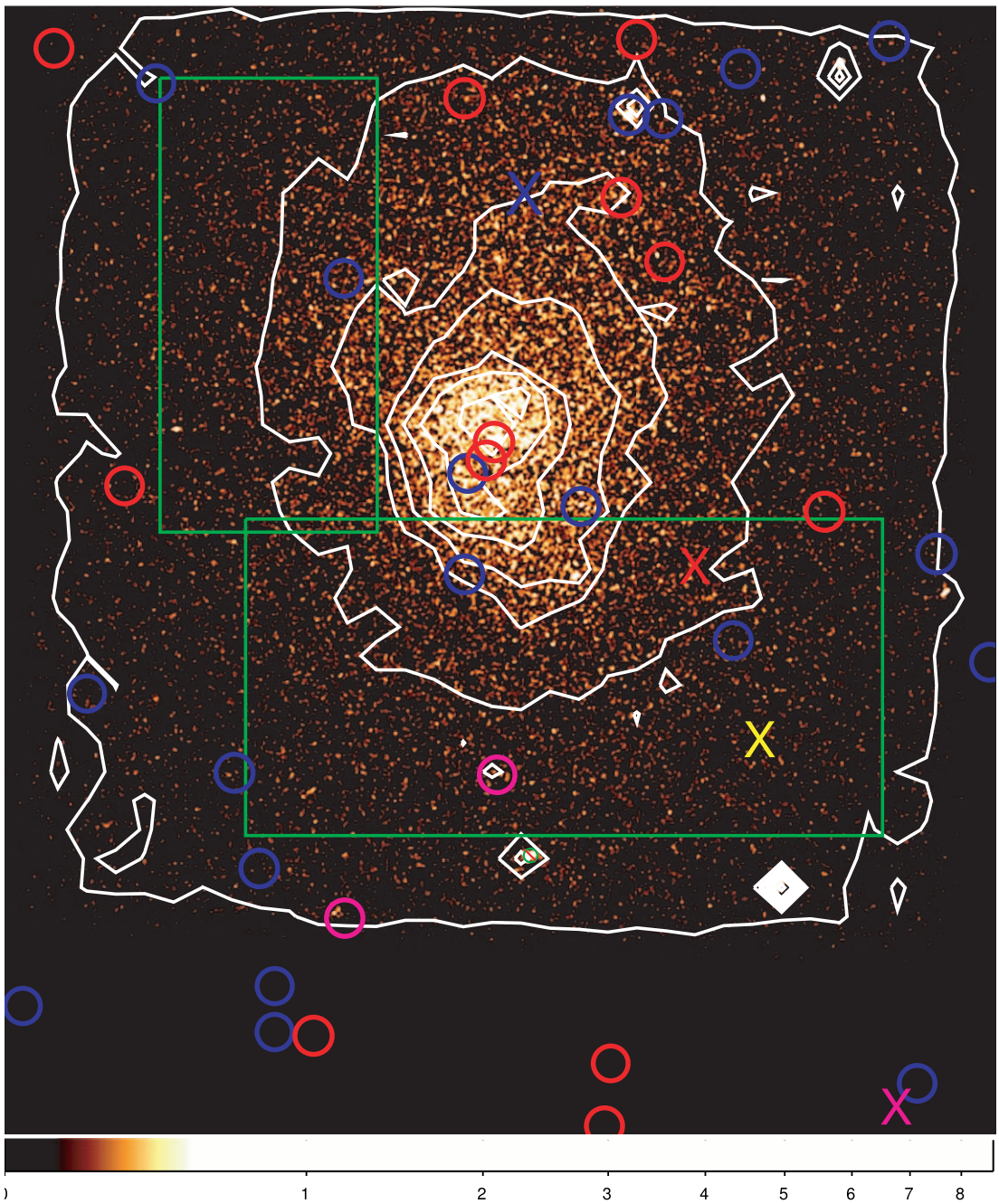

FIG. 6c

scales equivalent to the virial radius of a 4 keV cluster, $r_{200} \sim 0.85(kT_{\rm keV})^{1/2}\ h_{70}^{-1}$ Mpc $= 1.7\ h_{70}^{-1}$ Mpc, finds 3.9×10^4 in 5×10^5 clusters, i.e., a probability of 0.078. This estimate includes pairs of all relative velocities, but a recent analysis of velocity differences between subhalos and host halos found for Bullet Cluster (1E 0657−56; Markevitch et al. 2002) type halos in the Millennium simulation (Hayashi & White 2006) indicates that large velocity differences are not uncommon. They find that 40% of all host halos would have 1 of the 10 most massive subhalos with a velocity as high as that of the Bullet Cluster. From these studies, we roughly estimate that the likelihood of an ongoing merger with sufficiently high relative velocity is at the 1% level, and thus a few examples in the local population of observed massive clusters should be expected.

The distributions of gas temperature, iron abundance, and abundance ratios suggest that the merging axis component on the plane of the sky would follow a northwest-southeast direction. The best configuration that explains the magnitude of the velocity gradient is a scenario similar to that of the Bullet Cluster (1E 0657−56), i.e., a violent merger of two colder clusters and a (initial) merger axis making $\sim 80^\circ$ with the plane of the sky and a small ($\sim 10^\circ$, see below) deviation with respect to the north-south direction.[6]

A major prediction of the merging scenario is the presence of a hot (>10 keV if we scale from 1E 0657−56) component

[6] The closest configuration with the bullet cluster would be a $\sim 180^\circ$ flip over the *X*-axis of Fig. 2 from Markevitch et al. (2002), where the observer is viewing from the right.

corresponding to the bow shock layer on the line of sight. In order to test the consistency of this prediction with the current data we extracted spectra from a large elliptical region surrounding the cluster's center covering the outer "temperature ring" seen in Figure 2*a* as dashed ellipses (but also including the center). We compared two spectral models fitting simultaneously five data sets, *XMM-Newton* MOS1 and MOS2 data from the two pointings and ACIS-S3 data. The first one (model 1) was a single-temperature WABS APEC. The second (model 2) was a double-temperature WABS(APEC + APEC) corresponding to the cold and hot components. The cold component temperature was fixed at 3.5 keV, the lowest temperature observed throughout the temperature map. The normalization of the hot component was fixed at a fraction, $f_{\rm norm}$, of that of the cold component. The number of degrees of freedom in the two models is the same given the constraints imposed on the double-temperature component. We varied $f_{\rm norm}$ from 1% to 99% and recorded the best-fit parameters. The results are shown in Figure 7*a*, where we plot the χ^2 distribution as a function of $f_{\rm norm}$. It can be seen that the lowest χ^2 is achieved at $\sim$25% with a corresponding high temperature of 11.8 keV $< T <$ 21 keV at the 1 σ level. From Figure 7*a* we can see that the model 2 spectral fitting with $f_{\rm norm} \gtrsim 12\%$ is better than that using a single-temperature component (model 1), which has a χ^2 of 1407 and is shown in Figure 7*a* as a straight line with a best-fit temperature of 4.1 keV.

For comparison, we estimated the fractional contribution of the hot component using a recently archived 100 ks *Chandra* exposure of 1E 0657−56 (ObsID 5356). In Figure 7*b* we show the raw X-ray image and the rectangular region used to extract a surface brightness profile along the main direction of motion of the "bullet" to estimate the relative emission measure. The width of the rectangular region ($\sim$25″) corresponds to a $\sim$3′ region in Abell 576. In Figure 7*c* we show the surface brightness profile along the slice. From right to left the first surface brightness enhancement before the "spike" associated with the cool bullet is that of the shock region ($\sim$240″–280″). Then we see the colder bullet followed by an extended peak of the disturbed core of the primary cluster ($\sim$100″–240″). The last component is a hot tail ($\sim$20″–100″). We separated the regions into three parts based on the temperature map in Markevitch et al. (2002). The distribution of photon counts for these three components (again from right to left) is approximately 1000 counts (shock region), 14,500 counts (the two cold cores), and 3000 counts (hot tail), which would place the $f_{\rm norm}$ (hot/cold) at $\sim$26% assuming that the bow shock symmetrically covers the two cluster cores. This fraction can be directly compared to that derived using spectral fittings up to the precision of a (weak) function of temperature $f(T)$:

$$\begin{aligned}\text{number counts} &\propto \text{projected area} \times \text{surface brightness}\\ &\propto \text{density}^2 \times f(T) \times \text{projected area}\\ &\propto \frac{\text{normalization}_{\rm VAPEC}}{\text{characteristic size}} \times f(T).\end{aligned}$$

It is beyond the scope of this paper to carry out detailed modeling of 1E 0657−56. Nevertheless, we point out that the overall agreement of $f_{\rm norm}$ with what would be expected from "seeing" the Bullet Cluster along the merging axis is very consistent with Abell 576 passing through a near line-of-sight collision.

With the available data we do not have enough photon statistics and energy coverage to disentangle the multiple temperature components in the line of sight, i.e., cold gas from the preshocked ICM, a relatively thin bow shock, the projected high-density cold cores, and finally the post- and preshocked material at the largest

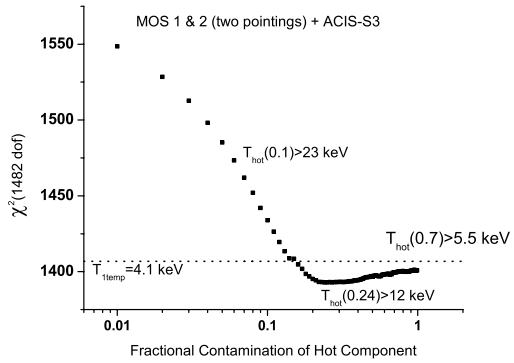

FIG. 7*a*

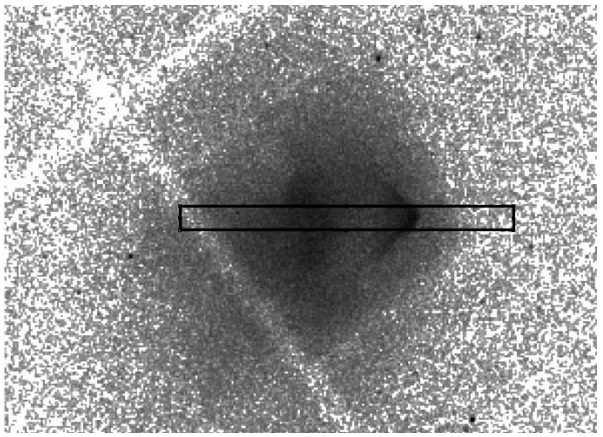

FIG. 7*b*

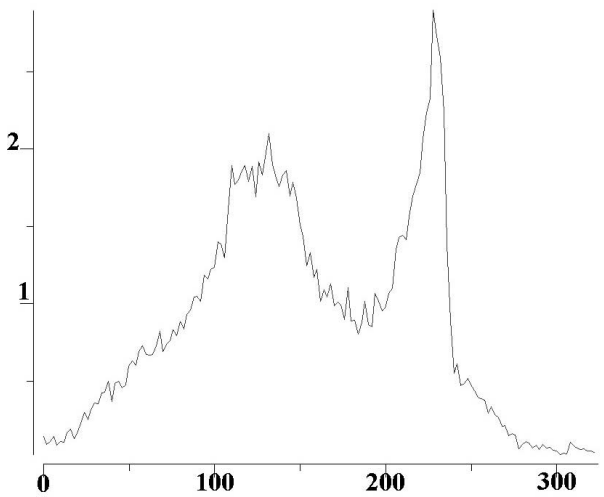

FIG. 7*c*

FIG. 7.—(*a*) The χ^2 variation of the best-fit double-APEC model to a large elliptical region encompassing the central regions of Abell 576 as a function of the ratio of normalizations of the hot to cold components. Intermediate values of the best-fit high temperatures are shown for normalization ratios of 10%, 24% (lowest χ^2), and 70%. The temperature of the cold component was fixed at 3.5 keV. The fit uses *XMM-Newton* MOS1 and MOS2 data from the two off-center pointings and ACIS-S3 data simultaneously. The dotted lines show the results for a single APEC with a best-fit temperature of 4.1 keV, for comparison. The number of degrees of freedom in the two models is the same given the constraints imposed on the double-temperature component. (*b*) ACIS-I image of 1E 0657−56 from a deep (100 ks) observation of the cluster. We also show the rectangular slice used to extract the surface brightness profile. North is up. The bright cross pattern centered in the top left of the figure is instrumental and should be neglected. (*c*) Surface brightness profile of the Bullet Cluster (1E 0657−56) along the rectangular slice shown in Fig. 7*b*. The *X*-axis is shown in arcseconds and the *Y*-axis in arbitrary surface brightness units. [*See the electronic edition of the Journal for a color version of this figure.*]

depth. However, we can roughly estimate a few merger parameters with the data at hand. From simple geometrical principles for a line-of-sight merger started at a time $-t_{\rm shock}$, the perturbation perpendicular to the surface of the Mach cone will propagate with the sound speed, so that $\cos\alpha = B/c_s t_{\rm shock}$, where α is half-angle of the cone, c_s is the sound speed given by $\left(5kT_{\rm ICM}/3\mu m_p\right)^{1/2} \approx 10^3[T_{\rm keV}/(3.7\ {\rm keV})]^{1/2}$ km s^{-1}, and B the projected distance from the merging axis to the point where the sonic perturbation is at a time $t_{\rm shock}$. Since the Mach number $M = 1/\sin\alpha$, the time when the shock front was effectively initiated is then $t_{\rm shock} = B/[c_s(1-M^{-2})^{1/2}]$ or $t_{\rm shock} \approx (0.08 \pm 0.015)\ h_{70}^{-1}$ Gyr ago, assuming B to be $B = 86 \pm 16\ h_{70}^{-1}$ kpc $\sim 1.75' \pm 0.5'$, where $2B \sim 3.5'$ would be the projected distance between the two "hot" regions (northwest and east of the central region) in Figure 2*a*. The distance traveled by the core along the line of sight during this time is $L \approx (0.45 \pm 0.15)\ h_{70}^{-1}$ Mpc for $M = 6 \pm 1.6$, using the error-weighted average velocity derived from *Chandra* and *XMM-Newton* data.

The point in the past that the two merging clusters overcome the Hubble flow, with zero relative radial velocity (half the orbital period), can be given by $r_0 = (2G/\pi^2)^{1/3}(M_c t_{\rm cross}^2)^{1/3} \approx 5.5(M_{c_{15}} t_{\rm cross_{Hub}}^2)^{1/3}$ Mpc, where $M_{c_{15}}$ is the total mass normalized by $10^{15}\ M_\odot$ and $t_{\rm cross_{Hub}}$ is the core crossing time normalized by a Hubble time (set to 1.37×10^{10} yr). From conservation of energy and angular momentum the relative velocity of the subsystems at a distance r from each other is given by (e.g., Ricker & Sarazin 2001)

$$v \sim \sqrt{2GM_c}\, r^{-1/2}\left[\frac{1 - r/r_0}{1 - (b/r_0)^2}\right]^{1/2} \approx 4160\sqrt{M_{c_{15}}}\, r_{0.5\ {\rm Mpc}}^{-1/2}\left[\frac{1 - r/r_0}{1 - (b/r_0)^2}\right]^{1/2}\ {\rm km\ s^{-1}},$$

where b is the impact parameter. If we use the distance between the X-ray peak and the midpoint between the two hot regions (=2B) in Figure 2*a* as the impact parameter we obtain $b = 50 \pm 25\ h_{70}^{-1}$ kpc. Taking the total mass (M_{500}) derived by R00, i.e., $M_c = (0.72 \pm 0.07) \times 10^{15}\ h_{70}^{-1}\ M_\odot$, the relative velocity at $r = L$, when the merger shock is effectively initiated, is found to be $(3.6 \pm 0.63) \times 10^3$ km s^{-1}. This value is in the lower end, but it is consistent, within the errors, with the observed velocity gradient, described in the previous paragraphs.

As pointed out by Dupke & Bregman (2002) and Sunyaev et al. (2003) ICM velocity detections can be corroborated by the use of the kinetic SZ effect (Sunyaev & Zel'dovich 1970, 1972, 1980). Intracluster gas bulk velocities as high as those detected in Abell 576 should generate significantly different levels of Comptonization of the cosmic microwave background radiation (CMBR) toward different directions of the cluster (redshifted and blueshifted sides). The total CMBR temperature variation toward the direction of a moving cluster has a thermal and a kinetic component:

$$\left(\frac{\Delta T}{T}\right)_\nu = \left[\frac{kT_e}{m_e c^2}\left(x\frac{e^x+1}{e^x-1} - 4\right) - \frac{V_r(b)}{c}\right]\tau, \qquad (1)$$

where T_e and T are the ICM and CMBR temperatures, respectively, V_r is the radial velocity, $x = h\nu/kT$, and the other parameters have their usual meanings (Sunyaev & Zel'dovich 1970, 1972, 1980). If the gas number density $n(r)$ follows a King-like profile $n(r) = n_0[1 + (r/r_c)^2]^{-(3/2)\beta}$, where r_c and n_0 are the core radius and the central density, respectively, the Thomson optical depth is given as a function of the projected radius $r_{\rm proj}$ by $\tau(r_{\rm proj}) = \sigma_{\rm T} n_0 r_c B(\frac{1}{2}, \frac{3}{2}\beta - \frac{1}{2})[1 + (r_{\rm proj}/r_c)^2]^{-(3/2)\beta+1/2}$, where $B(p,q) = \int_0^\infty x^{p-1}(1+x)^{p+q}\,dx$ is the beta function of p and q. Using $\beta = 0.64$, $r_c = 240\ h_{50}^{-1}$ kpc, and $n_0 = 2 \times 10^{-3}$ cm^{-3} (Mohr et al. 1996), $\tau \sim 1.3 \times 10^{-3}$ and from equation (1) we get $(\Delta T/T)_{217\ {\rm GHz}} = 2.6 \times 10^{-5}$, near the optimal frequency to observe the kinetic effect. This effect could be detected with current (or in development) instruments, such as the Bolocam,[7] ACBAR (Runyan et al. 2003), SuZIE (Holzapfel et al. 1997), or *Planck*.[8]

The low photon statistics limits our ability to fully disentangle the three-dimensional physics of the merging event to make a close comparison to theoretical/numerical models. However, this work suggests that the temperature, abundance, and velocity distributions in Abell 576 are consistent with a scenario in which the cluster is passing through a line-of-sight merger similar to that in the Bullet Cluster. If corroborated, this could provide a unique template to study supersonic line-of-sight cluster merger collisions. This work also illustrates the power of elemental abundance gradient distribution in determining the evolutionary stage of clusters.

The authors would like to thank Jimmy Irwin, Ed Lloyd-Davies, Maxim Markevitch, Chris Mullis, Kenneth Rines, Ming Sun, and Gastao Lima-Neto for useful discussions and suggestions. We also thank the anonymous referee for useful suggestions. We acknowledge support from NASA grant NAG5-3247. This research made use of the HEASARC *ASCA* database and NED. R. A. D. ackowledges partial support from FAPESP grant 06/05787-5.

[7] See http://www.astro.caltech.edu/~lgg/bolocam_front.htm.
[8] See http://www.rssd.esa.int/index.php?project=PLANCK&page=index.

REFERENCES

Allen, S. W., Fabian, A. C., Johnstone, R. M., Arnaud, K. A., & Nulsen, P. E. J. 2001, MNRAS, 322, 589
Anders, E., & Grevesse, N. 1989, Geochim. Cosmochim. Acta, 53, 197
Andersson, K. E., & Madejski, G. M. 2004, ApJ, 607, 190
Arnaud, K. A. 1996, in ASP Conf. Ser. 101, Astronomical Data Analysis Software and Systems V, ed. G. Jacoby & J. Barnes (San Francisco: ASP), 17
Baumgartner, W. H., Loewenstein, M., Horner, D. J., & Mushotzky, R. F. 2005, ApJ, 620, 680
Beers, T. 1982, ApJ, 257, 23
Benatov, L., Rines, K., Natarajan, P., Kravtsov, A., & Nagai, D. 2006, MNRAS, 370, 427
David, L. P., Slyz, A., Jones, C., Forman, W., Vrtilek, S. D., & Arnaud, K. A. 1993, ApJ, 412, 479
De Grandi, S., Ettori, S., Longhetti, M., & Molendi, S. 2004, A&A, 419, 7
Diaferio, A., & Geller, M. J. 1997, ApJ, 481, 633
Dupke, R. A. 1998, Ph.D. thesis, Univ. Alabama
Dupke, R. A., & Bregman, J. N. 2001a, ApJ, 547, 705
———. 2001b, ApJ, 562, 266
———. 2002, ApJ, 575, 634
———. 2005, ApJS, 161, 224 (DB05)
———. 2006, ApJ, 639, 781 (DB06)
Dupke, R. A., & White, R. E., III. 2000a, ApJ, 528, 139
———. 2000b, ApJ, 537, 123
———. 2003, ApJ, 583, L13
Evrard, A. E., et al. 2002, ApJ, 573, 7
Finoguenov, A., David, L. P., & Ponman, T. J. 2000, ApJ, 544, 188
Gibson, B. K., Loewenstein, M., & Mushotzky, R. F. 1997, MNRAS, 290, 623
Grant, C. 2001, ACIS Memo 195 (Cambridge: MIT), http://space.mit.edu/ACIS/ps_files/ps195.ps.gz
Hayashi, E., & White, S. D. M. 2006, MNRAS, 370, L38
Holzapfel, W. L., Wilbanks, T. M., Ade, P. A. R., Church, S. E., Fischer, M. L., Mauskopf, P. D., Osgood, D. E., & Lange, A. E. 1997, ApJ, 479, 17

Hwang, H. S., & Lee, M. G. 2007, ApJ, 662, 236
Inogamov, N. A., & Sunyaev, R. A. 2003, Astron. Lett., 29, 791
Kay, S. T., Thomas, P. A., Jenkins, A., & Pearce, F. R. 2004, MNRAS, 355, 1091
Kempner, J., & David, L. 2004, ApJ, 607, 220 (KD04)
Loewenstein, M., & Mushotzky, R. F. 1996, ApJ, 466, 695
Markevitch, M., et al. 2002, ApJ, 567, 27
Mohr, J. J., Geller, M. J., Fabricant, D. G., Wegner, G., Thorstensen, J., & Richstone, D. O. 1996, ApJ, 470, 724
Morrison, R., & McCammon, D. 1983, ApJ, 270, 119
Mushotzky, R. F., Loewenstein, M., Arnaud, K. A., Tamura, T., Fukazawa, Y., Matsushita, K., Kikuchi, K., & Hatsukade, I. 1996, ApJ, 466, 686
Nomoto, K., Hashimoto, M., Tsujimoto, T., Thielemann, F.-K., Kishimoto, N., & Kubo, Y. 1997a, Nucl. Phys. A, 616, 79
Nomoto, K., Iwamoto, K., Nakasato, N., Thielemann, F.-K., Brachwitz, F., Tsujimoto, T., Kubo, Y., & Kishimoto, N. 1997b, Nucl. Phys. A, 621, 467
Ota, N., et al. 2007, PASJ, 59, 351
Pawl, A., Evrard, A., & Dupke, R. 2005, ApJ, 631, 773
Rasia, E., Tormen, G., & Moscardini, L. 2004, MNRAS, 351, 237
Rasia, E., et al. 2006, MNRAS, 369, 2013
Ricker, P. M., & Sarazin, C. 2001, ApJ, 561, 621
Rines, K., & Diaferio, A. 2006, AJ, 132, 1275
Rines, K., Geller, M. J., Diaferio, A., Mohr, J. J., & Wegner, G. A. 2000, AJ, 120, 2338 (R00)
Rines, K., Geller, M. J., Kurtz, M., & Diaferio, A. 2003, AJ, 126, 2152
Rothenflug, R., Vigroux, L., Mushotzky, R. F., & Holt, S. S. 1984, ApJ, 279, 53
Runyan, M. C., et al. 2003, ApJS, 149, 265
Smith, R. J., Lucey, J. R., Hudson, M. J., Schlegel, D. J., & Davies, R. L. 2000, MNRAS, 313, 469
Sunyaev, R. A., Norman, M. L., Bryan, G. L. 2003, Astron. Lett., 29, 783
Sunyaev, R. A., & Zel'dovich, Ya. B. 1970, Ap&SS, 7, 3
———. 1972, Comments Astrophys. Space Phys., 4, 173
———. 1980, MNRAS, 190, 413
Wojtak, R., & Lokas, E. L. 2007, MNRAS, 377, 843